Galerkin/Collocation methods based on 1D-integrated-RBFNs for viscoelastic flows

D. Ho-Minh[1], **N. Mai-Duy**[1] **and T. Tran-Cong**[1]

Abstract: In this paper, one-dimensional integrated radial-basis-function networks (1D-IRBFNs) are introduced into the Galerkin and point-collocation formulations to simulate viscoelastic flows. The computational domain is represented by a Cartesian grid and IRBFNs, which are constructed through integration, are employed on each grid line to approximate the field variables including stresses in the streamfunction-vorticity formulation. Two types of fluid, namely Oldroyd-B and CEF models, are considered. The proposed methods are validated through the numerical simulation of several benchmark test problems including flows in a rectangular duct and in a corrugated tube. Numerical results show that accurate results are obtained using relatively-coarse grids.

Keywords: viscoelastic flows, Cartesian grid, 1D integrated RBFNs, point collocation, Galerkin formulation.

1 Introduction

Numerical simulation of viscoelastic flows still faces a lot of challenges. Main difficulties, which numerical methods have to deal with, are (i) complex material properties of fluids, (ii) mixed characters (elliptic for momentum equations and hyperbolic for constitutive equations), and (iii) high degrees of freedom (DOF) (2D problems: 6 DOFs/node and 3D problems: 10 DOFs/node). In the case of large deformations, free/moving surfaces and complex geometries, further numerical difficulties will be added. One can classify discretisation methods into two categories: low order and high order. The former, e.g. traditional finite difference (FDMs), finite element (FEMs), finite volume (FVMs) and boundary element (BEMs) methods, leads to a system matrix that is generally sparse and banded (possibly block-banded BEM), while the latter, e.g. spectral and RBFN methods, can offer a significant saving on the computational cost owing to their high-order rates of convergence. Further details can be found in [Crochet and Walters (1983); Crochet, Davies, and Walters (1984); Crochet (1989); Tanner and Xue (2002); Owens and Phillips (2002)].

The use of RBFNs for solving ordinary (ODEs) and partial (PDEs) differential equations has been an active research area since Kansa's first report in 1990 [Kansa (1990)]. For Kansa's method (direct approach), the field variable f in the ODE/PDE is first represented by an RBFN and this RBFN is then differentiated to obtain approximate expressions for derivative functions of f (differentiated RBFNs (DRBFN)). On the other hand,

---

[1] Computational Engineering and Science Research Centre (CESRC), Faculty of Engineering and Surveying (FoES), The University of Southern Queensland, Toowoomba, QLD 4350, Australia.

in order to avoid the reduction in convergence rate caused by differentiation, Mai-Duy and Tran-Cong (2001) proposed an indirect approach in which the highest-order derivatives of f are first decomposed into RBFs, and their lower-order derivatives and the function f itself are then obtained through integration (integrated RBFN (IRBFN)). Numerical experiments (e.g. [Mai-Duy and Tran-Cong (2001, 2003)]) showed that IRBFN collocation methods yield better accuracy than DRBFN ones for both the representation of functions and the solution of PDEs. In the early stages, both direct and indirect approaches used every RBF to construct the approximations for the field variable at a nodal point, leading to a fully-populated system matrix. It was found that the matrix condition number grows rapidly with respect to the increase in the RBF width and/or the number of RBFs [Schaback (1995)]. Global RBF solutions to steady viscoelastic flows were reported in, e.g., [Tran-Cong, Mai-Duy, and Phan-Thien (2002); Tran-Canh and Tran-Cong (2002); Mai-Duy and Tanner (2006)]. Later on, local RBF techniques, where the approximations are constructed using only a few nodal points, have been developed (e.g. [Atluri, Han, and Shen (2003); Atluri, Han, and Rajendran (2004); Sǎrler (2005); Mai-Duy and Tran-Cong (2009); Sellountos, Sequeira, and Polyzos (2010)]). In the context of IRBFNs, collocation schemes, based on 1D-IRBFNs and Cartesian grids, for the solution of 2D elliptic PDEs were reported in, e.g., [Mai-Duy and Tran-Cong (2007)]. The 1D-IRBFN approximations at a grid node involve only nodal points that lie on the grid lines intersecting at that point rather than the whole set of nodes. As a result, the construction process is conducted for a series of small matrices rather than for a large single matrix (thus some degree of local approximation is achieved).

1D-IRBFNs were successfully introduced into the point-collocation and Galerkin formulations for the simulation of heat transfer and Newtonian-fluid flows (e.g. [Mai-Duy and Tran-Cong (2007); Mai-Duy, Ho-Minh, and Tran-Cong (2009); Ho-Minh, Mai-Duy, and Tran-Cong (2009)]). It was shown that those methods are stable, accurate and converge well. The 1D-IRBFN-based Galerkin method can obtain similar levels of accuracy for both types of boundary condition, i.e. Dirichlet only and Dirichlet-Neumann. In addition, its resultant system of algebraic equations is often symmetric and has a relatively-low condition number, which facilitates the employment of a much larger number of nodes.

In this paper, we develop two methods (point collocation and Galerkin), which are based on 1D-IRBFNs and Cartesian grids, for the simulation of flows of viscoelastic fluids. The governing equations are taken in the streamfunction-vorticity formulation. A computational boundary condition for the vorticity is globally derived with the help of the constants of integration [Ho-Minh, Mai-Duy, and Tran-Cong (2009)]. Three benchmark test problems are considered to validate the proposed methods. In the first problem, fully-developed flows of an CEF fluid in a rectangular duct are simulated. This problem is widely used to study secondary flows in a straight tube of non-circular cross-section. It is noted that CEF is seen as an attractive constitutive model in the numerical modelling of polymer flow systems owing to its low computational cost [Criminale, Ericksen, and Filbey (1957)]. The second problem is concerned with the simulation of Poiseuille flows in a straight tube of circular cross-section, where their analytic solutions are available. The third problem is about the motion of an Oldroyd-B fluid in a corrugated tube - a standard test problem for numerical methods in non-Newtonian Fluid Mechanics [Burdette, Coates, Armstrong, and Brown (1989)]. In addition, this problem is also regarded as one of effective models in the study of viscoelastic flows in porous media. The obtained 1D-IRBFN results agree well with those produced by other techniques available in the literature.

The remainder of this paper is organised as follows. In Section 2, a brief review of the governing equations for the motion of CEF and Oldroyd-B fluids is given. Section 3 presents the proposed 1D-IRBFN-based Galerkin/collocation methods. Three test problems are simulated in Section 4. Section 5 concludes the paper.

2 Governing equations

The equations for the conservation of momentum and mass of an incompressible fluid take the forms

$$\rho \left(\frac{\partial \mathbf{v}}{\partial t} + \mathbf{v} \cdot \nabla \mathbf{v} \right) = \nabla \cdot \sigma + \mathbf{f}, \qquad \mathbf{x} \in \Omega, \tag{1}$$

$$\nabla \cdot \mathbf{v} = 0, \qquad \mathbf{x} \in \Omega, \tag{2}$$

where $\mathbf{v}$ is the velocity vector, $\mathbf{f}$ the body force vector per unit volume, ρ the density, σ the Cauchy stress tensor, t the time, $\mathbf{x}$ the position vector and Ω the domain of interest. The stress tensor can be decomposed into

$$\sigma = -p\mathbf{I} + \tau, \tag{3}$$

where p is the pressure, $\mathbf{I}$ the unit tensor and τ the extra stress tensor. In this paper, the working fluids are of the CEF and Oldroyd-B types.

For the CEF model, the extra stress tensor is defined as

$$\tau = 2\mu\left(d\right)\mathbf{d} - \Phi_1 \overset{\nabla}{\mathbf{d}} + 4\Phi_2 \mathbf{d} \cdot \mathbf{d}, \tag{4}$$

where $\mathbf{d} = 1/2(\nabla \mathbf{v} + (\nabla \mathbf{v})^T)$ is the rate of deformation tensor, $d = \sqrt{2tr(\mathbf{d} \cdot \mathbf{d})}$ the scalar magnitude of $\mathbf{d}$ (tr the trace operation), $\mu\left(d\right) = k|d|^{n-1}$ the viscosity (k the consistency factor and n the power law index), Φ_1 and Φ_2 the first and the second normal stress coefficients, respectively, and $\overset{\nabla}{[\,]}$ the upper convected derivative given by

$$\overset{\nabla}{[\,]} = \frac{\partial [\,]}{\partial t} + \mathbf{v} \cdot \nabla[\,] - (\nabla \mathbf{v})^T \cdot [\,] - [\,] \cdot \nabla \mathbf{v}. \tag{5}$$

For the Oldroyld-B model, the extra stress tensor is computed as

$$\tau = 2\mu_n \mathbf{d} + \tau_v, \tag{6}$$

$$\tau_v + \lambda \overset{\nabla}{\tau_v} = 2\mu_p \mathbf{d}, \tag{7}$$

where μ_n is the "Newtonian-contribution" viscosity, μ_p the "polymer-contribution" viscosity, τ_v the extra stress tensor due to viscoelasticity, and λ the relaxation time of the fluid. The Oldroyd-B model reduces to the UCM model when μ_n is set to zero and to the Newtonian model when $\lambda = 0$.

In this study, we consider the steady state of flows only and adopt the streamfunction-vorticity formulation. Eq. 1 - Eq. 3 thus reduce to

$$\nabla^2 \psi + \omega = 0, \tag{8}$$
$$\nabla^2 \omega = F(\mathbf{v} \cdot \nabla \omega, \tau, \mathbf{f}), \tag{9}$$

where ψ is the streamfunction, ω the vorticity, and the RHS of Eq. 9 the function of $\mathbf{v}$, ω, τ and $\mathbf{f}$. Numerical examples to be presented are solved in two coordinate systems, namely Cartesian and cylindrical.

The velocity components are related to the streamfunction via

$$u_x = -\frac{\partial \psi}{\partial y}, \quad u_y = \frac{\partial \psi}{\partial x} \quad \text{(Cartesian coordinates)}, \tag{10}$$

$$u_r = -\frac{1}{r}\frac{\partial \psi}{\partial z}, \quad u_z = \frac{1}{r}\frac{\partial \psi}{\partial r} \quad \text{(cylindrical coordinates)}. \tag{11}$$

For the CEF model, simulations are to be carried out using Cartesian coordinates and Eq. 4 is taken in the form

$$T_{xx} = 2\mu d_{xx} - \Phi_1 \left(u_x \frac{\partial d_{xx}}{\partial x} + u_y \frac{\partial d_{xx}}{\partial y} + \frac{\partial u_x}{\partial x} d_{xx} + \frac{\partial u_y}{\partial x} d_{xy} + \frac{\partial u_z}{\partial x} d_{xz} + d_{xx} \frac{\partial u_x}{\partial x} \right.$$
$$\left. + d_{xy} \frac{\partial u_y}{\partial x} + d_{xz} \frac{\partial u_z}{\partial x} \right) + (\Phi_1 + 4\Phi_2) \left(d_{xx}^2 + d_{xy}^2 + d_{xz}^2 \right), \tag{12}$$

$$T_{xy} = 2\mu d_{xy} - \Phi_1 \left(u_x \frac{\partial d_{xy}}{\partial x} + u_y \frac{\partial d_{xy}}{\partial y} + \frac{\partial u_x}{\partial x} d_{xy} + \frac{\partial u_y}{\partial x} d_{yy} + \frac{\partial u_z}{\partial x} d_{yz} + d_{xx} \frac{\partial u_x}{\partial y} \right.$$
$$\left. + d_{xy} \frac{\partial u_y}{\partial y} + d_{xz} \frac{\partial u_z}{\partial y} \right) + (\Phi_1 + 4\Phi_2) \left(d_{xx}d_{xy} + d_{xy}d_{yy} + d_{xz}d_{yz} \right), \tag{13}$$

$$T_{xz} = 2\mu d_{xz} - \Phi_1 \left(u_x \frac{\partial d_{xz}}{\partial x} + u_y \frac{\partial d_{xz}}{\partial y} + \frac{\partial u_x}{\partial x} d_{xz} + \frac{\partial u_y}{\partial x} d_{yz} + \frac{\partial u_z}{\partial x} d_{zz} + d_{xx} \frac{\partial u_x}{\partial z} \right.$$
$$\left. + d_{xy} \frac{\partial u_y}{\partial z} + d_{xz} \frac{\partial u_z}{\partial z} \right) + (\Phi_1 + 4\Phi_2) \left(d_{xx}d_{xz} + d_{xy}d_{yz} + d_{xz}d_{zz} \right), \tag{14}$$

$$T_{yy} = 2\mu d_{yy} - \Phi_1 \left(u_x \frac{\partial d_{yz}}{\partial x} + u_y \frac{\partial d_{yz}}{\partial y} + \frac{\partial u_x}{\partial y} d_{yx} + \frac{\partial u_y}{\partial y} d_{yy} + \frac{\partial u_z}{\partial y} d_{yz} + d_{xy} \frac{\partial u_x}{\partial y} \right.$$
$$\left. + d_{yy} \frac{\partial u_y}{\partial y} + d_{yz} \frac{\partial u_z}{\partial y} \right) + (\Phi_1 + 4\Phi_2) \left(d_{yx}^2 + d_{yy}^2 + d_{yz}^2 \right), \tag{15}$$

$$T_{yz} = 2\mu d_{yz} - \Phi_1 \left(u_x \frac{\partial d_{yz}}{\partial x} + u_y \frac{\partial d_{yz}}{\partial y} + \frac{\partial u_x}{\partial y} d_{xz} + \frac{\partial u_y}{\partial y} d_{yz} + \frac{\partial u_z}{\partial y} d_{zz} + d_{xy} \frac{\partial u_x}{\partial y} \right.$$
$$\left. + d_{yy} \frac{\partial u_y}{\partial y} + d_{yz} \frac{\partial u_z}{\partial y} \right) + (\Phi_1 + 4\Phi_2) \left(d_{yx}d_{xz} + d_{yy}d_{yz} + d_{yz}d_{zz} \right), \tag{16}$$

6

where

$$\mu = k \left(2 \left(\left(\frac{\partial u_x}{\partial x} \right)^2 + \left(\frac{\partial u_y}{\partial y} \right)^2 \right) + \left(\frac{\partial u_x}{\partial y} + \frac{\partial u_y}{\partial x} \right)^2 + \left(\frac{\partial u_z}{\partial x} \right)^2 + \left(\frac{\partial u_z}{\partial y} \right)^2 \right)^{\left(\frac{n-1}{2} \right)}, \tag{17}$$

and

$$\begin{bmatrix} d_{xx} & d_{xy} & d_{xz} \\ d_{yx} & d_{yy} & d_{yz} \\ d_{zx} & d_{zy} & d_{zz} \end{bmatrix} = \begin{bmatrix} \frac{\partial u_x}{\partial x} & \frac{1}{2} \left(\frac{\partial u_x}{\partial y} + \frac{\partial u_y}{\partial x} \right) & \frac{1}{2} \left(\frac{\partial u_x}{\partial z} + \frac{\partial u_z}{\partial x} \right) \\ \frac{1}{2} \left(\frac{\partial u_y}{\partial x} + \frac{\partial u_x}{\partial y} \right) & \frac{\partial u_y}{\partial y} & \frac{1}{2} \left(\frac{\partial u_y}{\partial z} + \frac{\partial u_z}{\partial y} \right) \\ \frac{1}{2} \left(\frac{\partial u_z}{\partial x} + \frac{\partial u_x}{\partial z} \right) & \frac{1}{2} \left(\frac{\partial u_z}{\partial y} + \frac{\partial u_y}{\partial z} \right) & \frac{\partial u_z}{\partial z} \end{bmatrix}. \tag{18}$$

The Oldroyd-B fluid flow is simulated using cylindrical coordinates and one thus has Eq. 7 in the form

$$T_{rr} + \lambda \left(u_r \frac{\partial T_{rr}}{\partial r} + u_z \frac{\partial T_{rr}}{\partial z} - 2 \left(\frac{\partial u_r}{\partial r} T_{rr} + \frac{\partial u_r}{\partial z} T_{rz} \right) \right) = 2\mu_p \frac{\partial u_r}{\partial r}, \tag{19}$$

$$T_{rz} + \lambda \left(u_r \frac{\partial T_{rz}}{\partial r} + u_z \frac{\partial T_{rz}}{\partial z} - \frac{\partial u_r}{\partial r} T_{rz} - \frac{\partial u_r}{\partial z} T_{zz} - \frac{\partial u_z}{\partial r} T_{rr} - \frac{\partial u_z}{\partial z} T_{rz} \right) = \mu_p \left(\frac{\partial u_r}{\partial z} + \frac{\partial u_z}{\partial r} \right), \tag{20}$$

$$T_{zz} + \lambda \left(u_r \frac{\partial T_{zz}}{\partial r} + u_z \frac{\partial T_{zz}}{\partial z} - 2 \left(\frac{\partial u_z}{\partial r} T_{rz} + \frac{\partial u_z}{\partial z} T_{zz} \right) \right) = 2\mu_p \frac{\partial u_z}{\partial z}, \tag{21}$$

$$T_{\theta\theta} + \lambda \left(u_r \frac{\partial T_{\theta\theta}}{\partial r} + u_z \frac{\partial T_{\theta\theta}}{\partial z} - 2 \frac{u_r}{r} T_{\theta\theta} \right) = 2\mu_p \frac{u_r}{r}. \tag{22}$$

3 Proposed 1D-IRBFN-based Galerkin/Collocation techniques

The computational domain is simply represented by a Cartesian grid. On each grid line, 1D-IRBFNs are employed to approximate the field variables, i.e. ψ, ω, T_{xx}, T_{xy}, T_{yy}, T_{xz}, T_{yz}, T_{rr}, T_{rz}, T_{zz} and $T_{\theta\theta}$. The governing equations Eq. 8 - Eq. 9, Eq. 12 - Eq. 16 and Eq. 19 - Eq. 22 are discretised by means of point collocation (the residual set to zero at the collocation points) or Galerkin formulation (the residual set to zero in the mean). In the following, details are presented for three main parts of the proposed methods. In the first part, the use of 1D-IRBFNs to represent the field variables is discussed. In the second part, the implementation of boundary conditions is described. In the third part, 1D-IRBFs are incorporated into the Galerkin and point-collocation formulations as the trial functions.

3.1 One-dimensional IRBFN representation of the field variables

It can be seen that Eq. 8 - Eq. 9 involve second-order derivatives of the field variables including stresses. As a result, the second-order integral RBF scheme [Mai-Duy and Tran-Cong (2003)] is applied in this work. Processes of constructing the 1D-IRBFN approximations for the field variables can be conducted in a similar fashion. For brevity, we introduce the notation f to represent ψ, ω, T_{xx}, T_{xy}, T_{yy}, T_{xz}, T_{yz}, T_{rr}, T_{rz}, T_{zz} or $T_{\theta\theta}$, and the notation η to denote x or y (Cartesian coordinates) and r or z (cylindrical coordinates).

On a η grid line, the field variable f and its derivatives with respect to η can be represented as follows.

$$\frac{d^2 f(\eta)}{d\eta^2} = \sum_{i=1}^{N_\eta} w_i g_i(\eta) = \sum_{i=1}^{N_\eta} w_i I_i^{(2)}(\eta), \tag{23}$$

$$\frac{d f(\eta)}{d\eta} = \sum_{i=1}^{N_\eta} w_i I_i^{(1)}(\eta) + c_1, \tag{24}$$

$$f(\eta) = \sum_{i=1}^{N_\eta} w_i I_i^{(0)}(\eta) + c_1 \eta + c_2, \tag{25}$$

where N_η is the number of nodes on the grid line, $\{w_i\}_{i=1}^{N_\eta}$ the set of network weights, $\{g_i(\eta)\}_{i=1}^{N_\eta} \equiv \left\{I_i^{(2)}(\eta)\right\}_{i=1}^{N_\eta}$ the set of RBFs, $I_i^{(1)}(\eta) = \int I_i^{(2)}(\eta) d\eta$, $I_i^{(0)}(\eta) = \int I_i^{(1)}(\eta) d\eta$, and c_1 and c_2 are the constants of integration. Evaluation of Eq. 23 - Eq. 25 at every node on the grid line leads to

$$\widehat{\frac{d^2 f}{d\eta^2}} = \widehat{\mathscr{I}}^{(2)} \widehat{\alpha}, \tag{26}$$

$$\widehat{\frac{df}{d\eta}} = \widehat{\mathscr{I}}^{(1)} \widehat{\alpha}, \tag{27}$$

$$\widehat{f} = \widehat{\mathscr{I}}^{(0)} \widehat{\alpha}, \tag{28}$$

where the superscript $(.)$ is used to denote the order of the corresponding derivative function,

$$\widehat{\mathscr{I}}^{(2)} = \begin{bmatrix} I_1^{(2)}(\eta_1), & I_2^{(2)}(\eta_1), & \cdots, & I_{N_\eta}^{(2)}(\eta_1), & 0, & 0 \\ I_1^{(2)}(\eta_2), & I_2^{(2)}(\eta_2), & \cdots, & I_{N_\eta}^{(2)}(\eta_2), & 0, & 0 \\ \vdots & \vdots & \ddots & \vdots & \vdots & \vdots \\ I_1^{(2)}(\eta_{N_\eta}), & I_2^{(2)}(\eta_{N_\eta}), & \cdots, & I_{N_\eta}^{(2)}(\eta_{N_\eta}), & 0, & 0 \end{bmatrix},$$

$$\widehat{\mathscr{I}}^{(1)} = \begin{bmatrix} I_1^{(1)}(\eta_1), & I_2^{(1)}(\eta_1), & \cdots, & I_{N_\eta}^{(1)}(\eta_1), & 1, & 0 \\ I_1^{(1)}(\eta_2), & I_2^{(1)}(\eta_2), & \cdots, & I_{N_\eta}^{(1)}(\eta_2), & 1, & 0 \\ \vdots & \vdots & \ddots & \vdots & \vdots & \vdots \\ I_1^{(1)}(\eta_{N_\eta}), & I_2^{(1)}(\eta_{N_\eta}), & \cdots, & I_{N_\eta}^{(1)}(\eta_{N_\eta}), & 1, & 0 \end{bmatrix},$$

$$\widehat{\mathscr{I}}^{(0)} = \begin{bmatrix} I_1^{(0)}(\eta_1), & I_2^{(0)}(\eta_1), & \cdots, & I_{N_\eta}^{(0)}(\eta_1), & \eta_1, & 1 \\ I_1^{(0)}(\eta_2), & I_2^{(0)}(\eta_2), & \cdots, & I_{N_\eta}^{(0)}(\eta_2), & \eta_2, & 1 \\ \vdots & \vdots & \ddots & \vdots & \vdots & \vdots \\ I_1^{(0)}(\eta_{N_\eta}), & I_2^{(0)}(\eta_{N_\eta}), & \cdots, & I_{N_\eta}^{(0)}(\eta_{N_\eta}), & \eta_{N_\eta}, & 1 \end{bmatrix},$$

$$\widehat{\alpha} = \left(w_1, w_2, \cdots, w_{N_\eta}, c_1, c_2\right)^T,$$

and

$$\widehat{\frac{d^k f}{d\eta^k}} = \left(\frac{d^k f_1}{d\eta^k}, \frac{d^k f_2}{d\eta^k}, \cdots, \frac{d^k f_{N_\eta}}{d\eta^k}\right)^T, \qquad k = \{1, 2\},$$

$$\widehat{f} = \left(f_1, f_2, \cdots, f_{N_\eta}\right)^T,$$

in which $d^k f_j/d\eta^k = d^k f(\eta_j)/d\eta^k$ and $f_j = f(\eta_j)$ with $j = \{1, 2, \cdots, N_\eta\}$.

The relations between the RBF-coefficient space $\widehat{\alpha}$ and the physical space $\widehat{f}$ can be established as

$$\begin{pmatrix} \widehat{f} \\ \widehat{e} \end{pmatrix} = \begin{bmatrix} \widehat{\mathscr{I}}^{(0)} \\ \widehat{\mathscr{K}} \end{bmatrix} \widehat{\alpha} = \widehat{\mathscr{C}}\widehat{\alpha}, \tag{29}$$

$$\widehat{\alpha} = \widehat{\mathscr{C}}^{-1} \begin{pmatrix} \widehat{f} \\ \widehat{e} \end{pmatrix}, \tag{30}$$

where $\widehat{e} = \widehat{\mathscr{K}}\widehat{\alpha}$ is used to represent extra information (derivative data), which would otherwise be wasted resulting in less accurate solutions, and $\widehat{\mathscr{C}}$ the conversion matrix. In Eq. 29 - Eq. 30, owing to the presence of the two integration constants, the vector $\widehat{e}$ can have up to two entries. Since the conversion matrix $\widehat{\mathscr{C}}$ is not over-determined, extra values e_i are incorporated into the IRBFN approximations in an exact manner. We will utilise this capability to impose normal derivative values at the two end-points of the grid line as well as to derive a computational boundary condition for the vorticity.

Making use of Eq. 30, the values of f and its derivatives at an arbitrary point η on the grid line will be computed

by

$$f(\eta) = \left(I_1^{(0)}(\eta), I_2^{(0)}(\eta), \cdots, I_{N_\eta}^{(0)}(\eta), \eta, 1\right) \widehat{\mathscr{C}}^{-1} \left(\begin{array}{c} \widehat{f} \\ \widehat{e} \end{array}\right), \tag{31}$$

$$\frac{\partial f(\eta)}{\partial \eta} = \left(I_1^{(1)}(\eta), I_2^{(1)}(\eta), \cdots, I_{N_\eta}^{(1)}(\eta), 1, 0\right) \widehat{\mathscr{C}}^{-1} \left(\begin{array}{c} \widehat{f} \\ \widehat{e} \end{array}\right), \tag{32}$$

$$\frac{\partial^2 f(\eta)}{\partial \eta^2} = \left(I_1^{(2)}(\eta), I_2^{(2)}(\eta), \cdots, I_{N_\eta}^{(2)}(\eta), 0, 0\right) \widehat{\mathscr{C}}^{-1} \left(\begin{array}{c} \widehat{f} \\ \widehat{e} \end{array}\right). \tag{33}$$

They can be rewritten in compact form

$$f(\eta) = \sum_{i=1}^{N_\eta} \varphi_i(\eta) f_i + \varphi_{N_\eta+1}(\eta) e_1 + \varphi_{N_\eta+2}(\eta) e_2, \tag{34}$$

$$\frac{\partial f(\eta)}{\partial \eta} = \sum_{i=1}^{N_\eta} \frac{\partial \varphi_i(\eta)}{\partial \eta} f_i + \frac{\partial \varphi_{N_\eta+1}(\eta)}{\partial \eta} e_1 + \frac{\partial \varphi_{N_\eta+2}(\eta)}{\partial \eta} e_2, \tag{35}$$

$$\frac{\partial^2 f(\eta)}{\partial \eta^2} = \sum_{i=1}^{N_\eta} \frac{\partial^2 \varphi_i(\eta)}{\partial \eta^2} f_i + \frac{\partial^2 \varphi_{N_\eta+1}(\eta)}{\partial \eta^2} e_1 + \frac{\partial^2 \varphi_{N_\eta+2}(\eta)}{\partial \eta^2} e_2, \tag{36}$$

where $\{\varphi_i\}_{i=1}^{N_\eta+2}$ is the set of IRBFN basis functions in the physical space.

3.2 Imposition of boundary conditions

Dirichlet boundary conditions: Assume that f is given at η_1 and η_{N_η}. In the conversion process, Eq. 29 - Eq. 30, the matrix $\widehat{\mathscr{K}}$ and the vector $\widehat{e}$ are simply set to null. The 1D-IRBFN expressions Eq. 34 - Eq. 36 thus reduce to

$$f(\eta) = \sum_{i=1}^{N_\eta} \varphi_i(\eta) f_i, \tag{37}$$

$$\frac{\partial f(\eta)}{\partial \eta} = \sum_{i=1}^{N_\eta} \frac{\partial \varphi_i(\eta)}{\partial \eta} f_i, \tag{38}$$

$$\frac{\partial^2 f(\eta)}{\partial \eta^2} = \sum_{i=1}^{N_\eta} \frac{\partial^2 \varphi_i(\eta)}{\partial \eta^2} f_i. \tag{39}$$

Neumann boundary conditions: Assume that $\partial f / \partial \eta$ is given at η_1 and η_{N_η}. The matrix $\widehat{\mathscr{K}}$ and the vector $\widehat{e}$ in Eq. 29 - Eq. 30 take the form

$$
\widehat{\mathscr{K}} = \left[\begin{array}{cccccc} I_1^{(1)}(\eta_1), & I_2^{(1)}(\eta_1), & \cdots, & I_{N_\eta}^{(1)}(\eta_1), & 1, & 0 \\ I_1^{(1)}(\eta_{N_\eta}), & I_2^{(1)}(\eta_{N_\eta}), & \cdots, & I_{N_\eta}^{(1)}(\eta_{N_\eta}), & 1, & 0 \end{array} \right],
$$

$$
\widehat{e} = \left(\begin{array}{c} \frac{\partial f_1}{\partial \eta} \\ \frac{\partial f_{N_\eta}}{\partial \eta} \end{array} \right).
$$

The 1D-IRBFN expressions Eq. 34 - Eq. 36 thus become

$$
f(\eta) = \sum_{i=1}^{N_\eta} \varphi_i(\eta) f_i + \varphi_{N_\eta+1}(\eta) \frac{\partial f_1}{\partial \eta} + \varphi_{N_\eta+2}(\eta) \frac{\partial f_{N_\eta}}{\partial \eta}, \tag{40}
$$

$$
\frac{\partial f(\eta)}{\partial \eta} = \sum_{i=1}^{N_\eta} \frac{\partial \varphi_i(\eta)}{\partial \eta} f_i + \frac{\partial \varphi_{N_\eta+1}(\eta)}{\partial \eta} \frac{\partial f_1}{\partial \eta} + \frac{\partial \varphi_{N_\eta+2}(\eta)}{\partial \eta} \frac{\partial f_{N_\eta}}{\partial \eta}, \tag{41}
$$

$$
\frac{\partial^2 f(\eta)}{\partial \eta^2} = \sum_{i=1}^{N_\eta} \frac{\partial^2 \varphi_i(\eta)}{\partial \eta^2} f_i + \frac{\partial^2 \varphi_{N_\eta+1}(\eta)}{\partial \eta^2} \frac{\partial f_1}{\partial \eta} + \frac{\partial^2 \varphi_{N_\eta+2}(\eta)}{\partial \eta^2} \frac{\partial f_{N_\eta}}{\partial \eta}. \tag{42}
$$

Dirichlet and Neumann boundary conditions: Assume that f and $\partial f / \partial \eta$ are given at η_1 and η_{N_η}, respectively. The latter is imposed by taking the matrix $\widehat{\mathscr{K}}$ and the vector $\widehat{e}$ in Eq. 29 - Eq. 30 as

$$
\widehat{\mathscr{K}} = \left[\begin{array}{cccccc} I_1^{(1)}(\eta_{N_\eta}), & I_2^{(1)}(\eta_{N_\eta}), & \cdots, & I_{N_\eta}^{(1)}(\eta_{N_\eta}), & 1, & 0 \end{array} \right],
$$

$$
\widehat{e} = \left(\begin{array}{c} \frac{\partial f_{N_\eta}}{\partial \eta} \end{array} \right).
$$

One thus has Eq. 34 - Eq. 36 in the form

$$
f(\eta) = \sum_{i=1}^{N_\eta} \varphi_i(\eta) f_i + \varphi_{N_\eta+1}(\eta) \frac{\partial f_{N_\eta}}{\partial \eta}, \tag{43}
$$

$$
\frac{\partial f(\eta)}{\partial \eta} = \sum_{i=1}^{N_\eta} \frac{\partial \varphi_i(\eta)}{\partial \eta} f_i + \frac{\partial \varphi_{N_\eta+1}(\eta)}{\partial \eta} \frac{\partial f_{N_\eta}}{\partial \eta}, \tag{44}
$$

$$
\frac{\partial^2 f(\eta)}{\partial \eta^2} = \sum_{i=1}^{N_\eta} \frac{\partial^2 \varphi_i(\eta)}{\partial \eta^2} f_i + \frac{\partial^2 \varphi_{N_\eta+1}(\eta)}{\partial \eta^2} \frac{\partial f_{N_\eta}}{\partial \eta}. \tag{45}
$$

3.3 Incorporating 1D-IRBFNs into Galerkin and point-collocation formulations

Each governing equation in Eq. 8 - Eq. 9, Eq. 12 - Eq. 16 and Eq. 19 - Eq. 22 can be rewritten in the following form

$$
\mathscr{L}(f) = 0, \qquad \mathbf{x} \in \Omega, \tag{46}
$$

where $\mathscr{L}$ is a differential operator. 1D-IRBFN expressions Eq. 34 - Eq. 36 are utilised here to construct the approximations for f over Ω. On a 2D rectangular domain, this construction process can simply be done by means of Kronecker products. The use of tensor products leads to, for instance,

$$f(x,y) \;=\; \sum_{i=1}^{N_x}\sum_{j=1}^{N_y} \varphi_i^{(x)}(x)\varphi_j^{(y)}(y)f_{i,j}, \tag{47}$$

for the case of Dirichlet boundary conditions only, and

$$f(x,y) = \sum_{i=1}^{N_x} \varphi_i^{(x)}(x)\left(\sum_{j=1}^{N_y} \varphi_j^{(y)}(y)f_{i,j} + \varphi_{N_y+1}^{(y)}(y)\frac{\partial f_{i,1}}{\partial y} + \varphi_{N_y+2}^{(y)}(y)\frac{\partial f_{i,N_y}}{\partial y} \right). \tag{48}$$

for the case of Dirichlet and Neumann boundary conditions (Dirichlet conditions prescribed on the two vertical boundaries while Neumann conditions on the two horizontal boundaries). In Eq. 47 and Eq. 48, $f_{i,j}$ is the value of the variable f at the intersection of the ith horizontal grid line and jth vertical grid line, and $\partial f_{i,1}/\partial y$ and $\partial f_{i,N_y}/\partial y$ are nodal boundary derivative values. The products $\varphi_i^{(x)}\varphi_j^{(y)}$ are usually referred to as the trial/basis/approximating functions.

It is noted that the independent variables x and y in Eq. 47 - Eq. 48 will be replaced with r and z if cylindrical coordinates are employed.

One can find the unknown nodal values of f by constructing a scheme to minimise the following residual

$$R = L(f). \tag{49}$$

This process can be stated mathematically as

$$\int_{\Omega} WRd\Omega = 0, \tag{50}$$

where W is the weighting function to be chosen. In the point-collocation approach, the weighting function is chosen as the Dirac delta function, i.e. $W_i = \delta(x - x_i)$. In the Galerkin approach, the weighting function is chosen from the set of trial functions, i.e. $W_i = \phi_i(\mathbf{x})$, and the volume integrals in Eq. 50 can be numerically evaluated using Gauss quadrature.

As mentioned earlier, Neumann boundary conditions are presently imposed in an exact manner. This is numerically demonstrated here through the solution of the following ODE

$$\frac{d^2 f}{dx^2} + f + x = 0, \quad 0 \le x \le 1, \tag{51}$$

subject to a Dirichlet and Neumann boundary condition at $x = 0$ and $x = 1$, respectively.

In the case of conventional Galerkin methods, the approximation for f can be constructed to satisfy the Dirichlet condition at $x = 0$. The Neumann boundary condition $df/dx = \overline{q}$ at $x = 1$ is imposed through the following

12

statement

$$\int_0^1 \left(\frac{df}{dx}\frac{dW}{dx} - (f+x)W \right) dx = [\overline{q}W]_{x=1}, \tag{52}$$

which is obtained by applying integration by parts on Eq. 50. As shown in [Brebbia, Telles, and Wrobel (1984)], by differentiating the approximate function f, one has

$$\frac{df}{dx}\bigg|_{x=1} = 1.22\text{E-}1 + (1 + 1.22\text{E-}1)\overline{q},$$

which clearly indicates that the Neumann boundary condition is imposed in an approximate manner.

In the present Galerkin technique, the IRBFN approximation is constructed to satisfy not only the Dirichlet condition at $x = 0$ but also the Neumann boundary condition $df/dx = \overline{q}$ at $x = 1$. Using Eq. 43, the solution f is expressed as

$$f(x) = \sum_{i=1}^{N_x} \varphi_i(x)f_i + \varphi_{N_x+1}(x)\bar{q}. \tag{53}$$

This approximation is then forced to satisfy the ODE through

$$\int_0^1 \left(\frac{d^2f}{dx} + f + x \right) W dx = 0, \tag{54}$$

from which one is able to obtain the nodal values of f. By differentiating Eq. 53, one has

$$\frac{df}{dx}\bigg|_{x=1} = \sum_{i=1}^{N_x} \frac{d\varphi_i(x=1)}{dx}f_i + \frac{d\varphi_{N_x+1}(x=1)}{dx}\bar{q}.$$

With $N_x = 5$, it reduces to

$$\frac{df}{dx}\bigg|_{x=1} = (\text{-}1.87\text{E-}14) + (1 + 5.07\text{E-}14)\overline{q} \simeq \overline{q},$$

which clearly shows that the Neumann boundary condition is imposed in an exact manner.

4 Numerical results

The proposed methods are validated through the simulation of viscoelastic flows in rectangular ducts (with Galerkin formulation), and in straight and corrugated tubes (point collocation). Fluid models under consideration here are CEF and Oldroyd-B. We employ uniform Cartesian grids to represent the computational domain and implement 1D-IRBFNs with the multiquadric (MQ) function

$$g_i(\eta) = \sqrt{(\eta - c_i)^2 + a_i^2}, \tag{55}$$

where c_i and a_i are the centre and the width/shape-parameter of the ith MQ-RBF, respectively. The latter is simply chosen to be the grid size.

4.1 Problem 1: Fully-developed flows of CEF fluid in rectangular ducts

The flow of a viscoelastic fluid in a rectangular duct has received a great deal of attention because of its fundamental and practical importance. Such a flow was simulated with different constitutive models (e.g. Reiner-Rivlin [Green and Rivlin (1956)], CEF [Gervang and Larsen (1991); Mai-Duy and Tanner (2006)] and modified PTT (MPTT) [Xue, Phan-Thien, and Tanner (1995)]). Results by Gervang and Larsen (1991), where the CEF model is employed and simulations are conducted both numerically and experimentally, are often cited in the literature for comparison purposes. In this study, we also consider the CEF model and its parameters are taken to be the same as those in [Gervang and Larsen (1991)]. The governing equations are expressed in terms of streamfunction, vorticity, pressure and primary velocity as

$$\frac{\partial^2 \psi}{\partial x^2} + \frac{\partial^2 \psi}{\partial y^2} + \omega = 0, \tag{56}$$

$$\mu \left(\frac{\partial^2 \omega}{\partial x^2} + \frac{\partial^2 \omega}{\partial y^2} \right) = \rho \left(\frac{\partial \psi}{\partial y} \frac{\partial \omega}{\partial x} - \frac{\partial \psi}{\partial x} \frac{\partial \omega}{\partial y} \right) - \frac{\partial^2 T_{xy}}{\partial x^2} + \frac{\partial^2 (T_{xx} - T_{yy})}{\partial x \partial y} + \frac{\partial^2 T_{xy}}{\partial y^2}, \tag{57}$$

$$\mu \left(\frac{\partial^2 u_z}{\partial x^2} + \frac{\partial^2 u_z}{\partial y^2} \right) = \frac{\partial p}{\partial z} + \rho \left(\frac{\partial \psi}{\partial y} \frac{\partial u_z}{\partial x} - \frac{\partial \psi}{\partial x} \frac{\partial u_z}{\partial y} \right) - \frac{\partial T_{zx}}{\partial x} - \frac{\partial T_{zy}}{\partial y}, \tag{58}$$

where the function F in Eq. 9 is now given explicitly. The flow is generated by a pressure drop $\partial p / \partial z$ and the computation domain is only a 2D region (cross-section) on the $x - y$ plane. Let χ be the aspect ratio. We consider four values of χ, namely 1, 1.56, 4 and 6.25.

Non-slip boundary conditions lead to $\psi = 0$, $u_z = 0$ and $\partial \psi / \partial n = 0$ on the wall (n is the coordinate direction normal to the wall). The condition $\partial \psi / \partial n = 0$ is used to derive a computational boundary condition for ω. This process is carried out here with the help of the integration constants; the reader is referred to our previous work [Ho-Minh, Mai-Duy, and Tran-Cong (2009)] for the detailed implementation. Eq. 56 - Eq. 58 for ψ, ω and u_z are thus all subject to Dirichlet boundary conditions.

We apply the Galerkin formulation to discretise the governing equations and a Picard iterative scheme to handle the resultant nonlinear system of algebraic equations. All the terms on the RHS of Eq. 57 and Eq. 58 are lumped together in the "pseudo-body forces". The solution procedure can be summarised as follows.

1. Discretise spatial derivatives using 1D-IRBFNs, resulting in a high-order approximation scheme in space

2. Guess values of ψ, ω and u_z, and their first-order spatial derivatives

3. Compute the pseudo-body forces and the boundary values for ω. It is noted that the CEF stress components are simply obtained through direct calculation of Eq. 12 - Eq. 16

4. Solve the coupled linearised governing equations Eq. 56 - Eq. 58, where the system matrix is generated from the linear terms on their LHS

5. Check to see whether the solution has reached a steady state

$$\frac{\sqrt{\sum_{i=1}^{N}\left(\psi_i^{(k)}-\psi_i^{(k-1)}\right)^2+\sum_{i=1}^{N}\left(\omega_i^{(k)}-\omega_i^{(k-1)}\right)^2+\sum_{i=1}^{N}\left(u_{zi}^{(k)}-u_{zi}^{(k-1)}\right)^2}}{\sqrt{\sum_{i=1}^{N}\left(\psi_i^{(k)}\right)^2+\sum_{i=1}^{N}\left(\omega_i^{(k)}\right)^2+\sum_{i=1}^{N}\left(u_{zi}^{(k)}\right)^2}}<\varepsilon,\tag{59}$$

where k indicates the iteration number and ε is a prescribed tolerance

6. If it is not satisfied, for every interior node, relax the solution fields

$$\psi_i = \gamma\psi_i^{(k)}+(1-\gamma)\,\psi_i^{(k-1)},\tag{60}$$
$$\omega_i = \gamma\omega_i^{(k)}+(1-\gamma)\,\omega_i^{(k-1)},\tag{61}$$
$$u_{zi} = \gamma u_{zi}^{(k)}+(1-\gamma)\,u_{zi}^{(k-1)},\tag{62}$$

where γ is the relaxation factor $(0<\gamma<1)$, and then repeat from step 3. Otherwise, stop the computation and output the results.

Computations are carried out using $\gamma=0.01$ and grids of $\{11\times11,21\times21,\cdots,61\times61\}$. Fig. 1 and Fig. 2 show the convergence behaviour of the streamfunction and vorticity fields at $\chi=1$, respectively. It can be seen that the flow is symmetric about the vertical and horizontal centreline and the two fields converge very fast with grid refinement. There are eight vortices in total, where secondary circulations have the same magnitude but different signs (i.e. one vortex is in opposite direction to its two adjacent vortices). Fig. 3 and Fig. 4 show patterns of the secondary flow for $\chi=\{1.56,4,6.25\}$ on one quarter of the cross-section. Each quadrant has two vortices, whose patterns and strength strongly depend on the aspect ratio for a given mean primary velocity. Unlike the case of $\chi=1$, where the two vortices are symmetric about the diagonal plane, the case of $\chi>1$ produces two vortices of different sizes. The vortex near the long wall moves towards the short wall with increasing χ, while the vortex near the short wall is reduced in size. Fig. 5 and Fig. 6 show patterns of the primary flow and the second normal stress difference for all aspect ratios. The 1D-IRBFN Galerkin results are similar to those reported in [Gervang and Larsen (1991); Xue, Phan-Thien, and Tanner (1995)].

4.2 *Problem 2: Fully-developed flows of Oldroyd-B fluid in circular tubes*

This problem is concerned with the so-called Poiseuille flow in a circular tube. Let R be the radius of the tube. The governing equations Eq. 1 - Eq. 2 and Eq. 19 - Eq. 22 are made dimensionless by scaling lengths by R, velocity components by Q/R^2, and stress components and pressure by $(\mu_n+\mu_p)Q/R^3$ in which Q is the flow rate. In a cylindrical coordinate system, the non-dimensional form of Eq. 8 - Eq. 9 for the motion of an

Oldroyd-B fluid is given by [Pilitsis and Beris (1989)]

$$\left(\frac{\partial^2 \psi}{\partial r^2} + \frac{\partial^2 \psi}{\partial z^2} - \frac{1}{r} \frac{\partial \psi}{\partial r} \right) + \omega = 0, \tag{63}$$

$$\alpha \left(\frac{\partial^2 \omega}{\partial r^2} + \frac{1}{r} \frac{\partial \omega}{\partial r} - \frac{\omega}{r^2} + \frac{\partial^2 \omega}{\partial z^2} \right) = \frac{\partial^2 T_{rz}}{\partial r^2} - \frac{\partial^2 T_{rr}}{\partial z \partial r} - \frac{\partial^2 T_{rz}}{\partial z^2}$$
$$- \frac{1}{r} \left(\frac{\partial T_{rr}}{\partial z} - \frac{\partial T_{\theta\theta}}{\partial z} \right) + \frac{\partial^2 T_{zz}}{\partial r \partial z} - \frac{1}{r^2} T_{rz} + \frac{1}{r} \frac{\partial T_{rz}}{\partial r}, \tag{64}$$

where $\alpha = \mu_n / (\mu_n + \mu_p)$ and the inertia terms are set aside. The velocity and stress fields can be obtained analytically and their exact forms are

$$\widetilde{u}_z = 1 - r^2, \ \widetilde{u}_r = 0, \tag{65}$$

$$\widetilde{T}_{zz} = We(1 - \alpha) \left(\frac{\partial \widetilde{u}_z}{\partial r} \right)^2, \ \widetilde{T}_{rz} = (1 - \alpha) \frac{\partial \widetilde{u}_z}{\partial r}, \ \widetilde{T}_{rr} = 0, \tag{66}$$

where $We = \lambda Q / R^3$ is the Weissenberg number. In the present simulation, the length and the radius of the tube are all chosen to be 1. Boundary conditions are prescribed as follows.

- On the centreline:

$$\psi = \omega = T_{rz} = \frac{\partial T_{rr}}{\partial r} = \frac{\partial T_{zz}}{\partial r} = \frac{\partial T_{\theta\theta}}{\partial r} = 0 \quad \text{(symmetrical conditions)}$$

- On the wall: Through Eq. 11 ($u_z = 1/r(\partial \psi/\partial r)$), the streamfunction value is determined as $\psi = Q/2\pi$. Given $Q = \pi/2$, one has $\psi = 1/4$. The vorticity value can be obtained using the same procedure as in Problem 1.

- On the inlet and the outlet:

$$\psi^i = \psi^o, \quad \frac{\partial \psi^i}{\partial n} = \frac{\partial \psi^o}{\partial n}, \quad \omega^i = \omega^o, \quad \frac{\partial \omega^i}{\partial n} = \frac{\partial \omega^o}{\partial n},$$

$$T_{rr}^i = T_{rr}^o, \quad T_{rz}^i = T_{rz}^o, \quad T_{zz}^i = T_{zz}^o, \quad T_{\theta\theta}^i = T_{\theta\theta}^o,$$

where periodicity is taken into account, and superscripts i and o denote the inlet and outlet, respectively.

Unlike Problem 1, the point-collocation formulation is employed here. We take $\alpha = 0.85$ and also apply a Picard iterative scheme to handle the nonlinearity of the system. Results obtained are presented in Tab. 1 and Fig. 7. Tab. 1 is concerned with the study of grid convergence at $We = 9$. Errors are consistently reduced as the grid density increases. Fig. 7 shows profiles of the velocity, the shear stress and the first normal stress difference on the middle plane ($z = 0.5$) for the Weissenberg number in the range of 0.5 to 10. It can be seen that the 1D-IRBFN collocation results agree well with the analytic solutions.

4.3 Problem 3: Flows of Newtonian and Oldroyd-B fluids in corrugated tubes

The 1D-IRBFN collocation method is further validated through the simulation of flows in corrugated tubes. It is well known that such flows, where their solutions are smooth and there are no inflow/outflow boundary conditions applied, are chosen as a benchmark test problem for validating new solvers in computational rheology. Solutions to these flows were reported for several numerical methods, e.g. the pseudospectral finite difference method (PSFD), pseudo-spectral cylindrical finite difference method (PCFD) and full pseudo-spectral method (FCC) by Pilitsis and Beris (1989, 1991, 1992), the spectral method (SM) by Momeni-Masuleh and Phillips (2004), EMME/FEM by Burdette, Coates, Armstrong, and Brown (1989); Rajagopalan, Armstrong, and Brown (1990), EVSS/FEM by Szady, Salamon, Liu, Bornside, and Armstrong (1995), BEM by Zheng, Phan-Thien, Tanner, and Bush (1990), and 2D-IRBFN by Mai-Duy and Tanner (2006).

Fig. 8a shows the flow geometry, where the radius of the corrugated tube along the z axis is given by

$$r_w = R(1 - \varepsilon \cos(2\pi z/L)), \tag{67}$$

where R is the average radius of an equivalent straight tube, ε the amplitude of the corrugation and L the wavelength. In addition to ε, two more characteristic dimensionless numbers are also used. They are the aspect ratio $N = R/L$ and the wave number l; their relation is $N = l/(2\pi)$. Since the flow is axisymmetric and periodic, only a reduced domain (Fig. 8b) needs be considered for the numerical study.

The streamfunction and vorticity equations as well as the boundary conditions here are similar to those in Problem 2. The governing equations are solved in a stretched cylindrical coordinate system $(\hat{r}, \theta, \hat{z})$, where $\hat{r} \equiv r/r_w$ and $\hat{z} \equiv z$. One important measure for corrugated tube flows is the flow resistance defined as

$$f\text{Re} = \frac{2\pi \Delta P R^4}{L(\mu_n + \mu_p)Q}, \tag{68}$$

where ΔP is the constant pressure drop per unit cell.

4.3.1 Newtonian fluid

The proposed method is first tested with the case of a Newtonian fluid. With the presence of the inertial term, the vorticity equation Eq. 9 becomes [Pilitsis and Beris (1991)]

$$\left(\frac{\partial^2 \omega}{\partial r^2} + \frac{1}{r}\frac{\partial \omega}{\partial r} - \frac{\omega}{r^2} + \frac{\partial^2 \omega}{\partial z^2} \right) = \frac{\pi Re}{2} \left(u_z \frac{\partial \omega}{\partial z} + u_r \frac{\partial \omega}{\partial r} - \frac{u_r}{r}\omega \right), \tag{69}$$

where Re is the Reynolds number defined as

$$Re = \frac{2\rho Q}{\pi R \mu}. \tag{70}$$

Results concerning $f\text{Re}$ for $Re = 0$ employed with several geometries by the present method and by SM, FCC, PSFD and PCFD are presented in Tab. 2. It can be seen that a good agreement is achieved for all cases. Fig. 9

shows streamlines for $\varepsilon = 0.5$ and $N = 0.5$, whose structure can be seen to be similar to that in [Pilitsis and Beris (1991)]. As expected, the streamfunction field is symmetric about the widest cross-section of the tube, i.e. $z = 1/2$.

For $Re > 0$, we consider the tube with ($\varepsilon = 0.16, N = 0.3$) and Re up to a value of 783. Tab. 3 reports fRe for a wide range of Re. Results obtained by the global spectral method [Lahbabi and Chang (1986)], and by the Galerkin finite element method (GFE) and FCC [Pilitsis and Beris (1992)] are also included for comparison purposes. The 1D-IRBFN results approach the FCC ones as the grid is refined. Furthermore, they are in better agreement with the FCC results than the GFE ones. Contour plots for the streamfunction and vorticity are shown in Fig. 10, which look feasible in comparison with those reported in [Lahbabi and Chang (1986); Mai-Duy and Tanner (2006)]. It can be seen that the flows are no longer symmetric. There appears a recirculation. As Re increases, its size grows and its centre moves towards the tube axis.

4.3.2 Oldroyd-B fluid

The Oldroyd-B model is implemented with $\alpha = 0.85$ that is widely used in the literature (e.g. [Pilitsis and Beris (1989)]). Like in [Pilitsis and Beris (1989)], we only consider creeping flows. Taking non-slip and symmetrical boundary conditions into account, the constitutive equations reduce to algebraic equations on the wall and to ODEs on the centreline, respectively. As a result, the stress equations on these boundary lines can be solved separately from the set of stress equations associated with the interior nodes. On the other hand, the value of u_z on the centreline can be obtained by means of L'Hospital's rule.

In this work, instead of considering ODEs, the values of T_{rr}, T_{zz} and $T_{\theta\theta}$ on the centreline are computed by directly employing 1D-IRBFNs (function interpolation). Those values are regarded as nodal unknowns and they can be found using the symmetric conditions. On each radial grid line z_i with $i = (2, \cdots, N_z - 1)$, through Eq. 38, one has

$$\frac{\partial T_{rr}(z_i, r = 0)}{\partial r} = \sum_{j=1}^{N_r} \frac{\partial \varphi_j(r = 0)}{\partial r}(T_{rr})_{i,j} = 0, \tag{71}$$

$$\frac{\partial T_{zz}(z_i, r = 0)}{\partial r} = \sum_{j=1}^{N_r} \frac{\partial \varphi_j(r = 0)}{\partial r}(T_{zz})_{i,j} = 0, \tag{72}$$

$$\frac{\partial T_{\theta\theta}(z_i, r = 0)}{\partial r} = \sum_{j=1}^{N_r} \frac{\partial \varphi_j(r = 0)}{\partial r}(T_{\theta\theta})_{i,j} = 0. \tag{73}$$

Eq. 71 - Eq. 73 need be solved in conjunction with the set of stress equations associated with the interior nodes. The advantage of this approach is that one can avoid computing velocity derivatives in the constitutive equations on the centreline. We apply a coupled approach to handle the governing equations, in which the resultant nonlinear algebraic set is solved by means of Newton iteration (trust region method).

In the case of moderate corrugation amplitude and small wave length ($\varepsilon = 0.1$, $N = 0.5$), simulations are carried out with four grids of 11×11, 21×21, 31×31 and 41×41. The obtained results are shown in Fig. 11 for velocity, Fig. 12 and Fig. 13 for stress, and Fig. 14a for flow resistance. In Fig. 11, the distribution of u_r at

18

We = 2 is plotted showing the influence of the grid size. As the grid is refined, the smoothness of the computed field is improved and the maximum and minimum values of u_r remain unchanged. A grid density of 21×21 appears to be sufficient for computing u_r at *We* = 2. Fig. 12 shows the behaviour of T_{rz} with increasing *We*. At high values of *We*, steep layers are formed in the area close to the wall. This behaviour can also be seen for T_{zz} as shown in Fig. 13. In Fig. 14a, the 1D-IRBFN solution is shown to converge up to *We* = 6 and the values of *f*Re are in good agreement with the benchmark solution [Pilitsis and Beris (1992)] (solutions in [Pilitsis and Beris (1992)] reported only for three values of *We*, namely 0, 1.2071 and 3.6213). Denser grids are required for higher-*We* solutions. It is noted that the two coarse grids, 11×11 and 21×21, fail to yield a convergent solution for high values of *We*.

In the case of moderate corrugation amplitude and moderate wave length ($\varepsilon = 0.1$, $N = 0.16$), three grids of 11×11, 21×21 and 31×31 are employed. The plot of *f*Re versus *We* is shown in Fig. 14b. It can be seen that a convergent *f*Re solution is obtained up to *We* = 7 using 11×11, *We* = 8 using 21×21, and *We* = 18 using 31×31. Other remarks here are similar to those in the previous case ($\varepsilon = 0.1$, $N = 0.5$).

5 Concluding remarks

In this paper, viscoelastic flows in rectangular ducts and in straight and corrugated tubes are simulated with 1D-IRBFN-based Galerkin/Collocation techniques. Instead of using low-order polynomials, the trial functions in the Galerkin and point-collocation formulations are presently implemented with 1D-IRBFs. Boundary treatments especially for those on the centreline using 1D-IRBFNs are discussed in detail. The 1D-IRBFN results, which are obtained for a wide range of the Weissenberg number, are in good agreement with the exact/numerical solutions available in the literature. Implementation of the constitutive equations in their matrix logarithm form for higher *We* solutions in the context of 1D-IRBFNs is currently under investigation and will be reported in future work.

References

Atluri, S. N.; Han, Z. D.; Rajendran, A. M. (2004): A New Implementation of the Meshless Finite Volume Method, Through the MLPG "Mixed" Approach. *CMES: Computer Modeling in Engineering & Sciences*, vol. 6 (6), pp. 491–514.

Atluri, S. N.; Han, Z. D.; Shen, S. (2003): Meshless Local Petrov-Galerkin (MLPG) Approaches for Solving the Weakly-Singular Traction & Displacement Boundary Integral Equations. *CMES: Computer Modeling in Engineering & Sciences*, vol. 4 (5), pp. 507–518.

Brebbia, C. A.; Telles, J. C. F.; Wrobel, L. C. (1984): *Boundary Element Techniques: Theory and Applications in Engineering* . Spring-Verlag Berlin, Heidelberg.

Burdette, S. R.; Coates, P. J.; Armstrong, R. C.; Brown, R. A. (1989): Calculations of viscoelastic flow through an axisymmetric corrugated tube using the explicitly elliptic momentum equation formulation (EEME). *Journal of Non-Newtonian Fluid Mechanics*, vol. 33, pp. 1–23.

Criminale, W. O. J.; Ericksen, J. L.; Filbey, G. L. J. (1957): Steady shear flow of non-Newtonian Fluids. *Archive for Rational Mechanics and Analysis*, vol. 1(1), pp. 410–417.

Crochet, M. J. (1989): Numerical simulation of viscoelastic flow: A review. *Rubber Chemistry and Technology*, vol. 62, pp. 426–455.

Crochet, M. J.; Davies, A. R.; Walters, K. (1984): *Numerical simulation of non-Newtonian flow*. Elsevier Science Publishers.

Crochet, M. J.; Walters, K. (1983): Numerical methods in non-Newtonian fluid mechanics. *Annual Review of Fluid Mechanics*, vol. 15, pp. 241–260.

Gervang, B.; Larsen, P. (1991): Secondary flows in straight ducts of rectangular cross section. *Journal of Non-Newtonian Fluid Mechanics*, vol. 39, pp. 217–237.

Green, G. E.; Rivlin, R. S. (1956): Steady flow of non-Newtonian fluids through tubes. *Quaterfly of Applied Mathematics*, vol. 14, pp. 299–308.

Ho-Minh, D.; Mai-Duy, N.; Tran-Cong, T. (2009): A Galerkin-RBF approach for the streamfunction-vorticity-temperature formulation of natural convection in 2D enclosured domains. *CMES: Computer Modeling in Engineering & Sciences*, vol. 44, pp. 219–248.

Kansa, E. J. (1990): Multiquadrics - A scattered data approximation scheme with applications to computational fluid dynamics I. Surface approximations and partial derivative estimates. *Computers and Mathematics with Applications*, vol. 19, pp. 127–145.

Lahbabi, A.; Chang, H. C. (1986): Flow in periodically constricted tubes: Transition to inertial and nonsteady flows. *Chemical Engineering Science*, vol. 41 (10), pp. 2487–2505.

Mai-Duy, N.; Ho-Minh, D.; Tran-Cong, T. (2009): A Galerkin approach incorporating integrated radial basis function networks for the solution of biharmonic equations in two dimensions. *International Journal of Computer Mathematics*, vol. 86 (10-11), pp. 1746–1759.

Mai-Duy, N.; Tanner, R. I. (2006): Computing non-Newtonian fluid flow with radial basis function networks. *International Journal for Numerical Methods in Fluids*, vol. 48, pp. 1309 –1336.

Mai-Duy, N.; Tran-Cong, T. (2001): Numerical solution of differential equations using multiquadric radial basis function networks. *Neural Networks*, vol. 14, pp. 185–199.

Mai-Duy, N.; Tran-Cong, T. (2003): Approximation of function and its derivatives using radial basis function network methods. *Applied Mathematical Modelling*, vol. 27, pp. 197–220.

Mai-Duy, N.; Tran-Cong, T. (2007): A Cartesian-grid collocation method based on radial basis function networks for solving PDEs in irregular domains. *Numerical Methods for Partial Differential Equations*, vol. 23, pp. 1192–1210.

Mai-Duy, N.; Tran-Cong, T. (2009): A Cartesian-Grid Discretisation Scheme Based on Local Integrated RBFNs for Two-Dimensional Elliptic Problems. *CMES: Computer Modeling in Engineering & Sciences*, vol. 51 (3), pp. 213–238.

Momeni-Masuleh, S. H.; Phillips, T. N. (2004): Viscoelastic flow in an undulating tube using spectral methods. *Computers & Fluids*, vol. 33, pp. 1075–1095.

Owens, R. G.; Phillips, T. N. (2002): *Computational Rheology*. Imperial College Press.

Phillips, T. N.; Owens, R. G. (1997): A mass conserving multi-domain spectral collocation method for the Stokes problem . *Computers & Fluids*, vol. 8, pp. 825–840.

Pilitsis, S.; Beris, A. N. (1989): Calculation of Steady-state viscoelastic flow in an undulating tube. *Journal of Non-Newtonian Fluid Mechanics*, vol. 31, pp. 231–287.

Pilitsis, S.; Beris, A. N. (1991): Viscoelastic flow in an undulating tube. Part II. Effects of high elasticity, large amplitude of undulation and inertia. *Journal of Non-Newtonian Fluid Mechanics*, vol. 39, pp. 375–405.

Pilitsis, S.; Beris, A. N. (1992): Pseudospectral calculations of viscoelastic flow in a periodically constricted tube . *Computer Methods in Applied Mechanics and Engineering*, vol. 98 (3), pp. 307–328.

Rajagopalan, D.; Armstrong, R. C.; Brown, R. A. (1990): Finite element methods for calculation of steady, viscoelastic flow using constitutive equations with a Newtonian viscosity. *Journal of Non-Newtonian Fluid Mechanics*, vol. 36, pp. 159–192.

Schaback, R. (1995): Error estimates and condition numbers for radial basis function interpolation. *Advances in Computational Mathematics*, vol. 3, pp. 251–264.

Sellountos, E. J.; Sequeira, A.; Polyzos, D. (2010): Solving Elastic Problems with Local Boundary Integral Equations (LBIE) and Radial Basis Functions (RBF) Cells. *CMES: Computer Modeling in Engineering & Sciences*, vol. 57 (2), pp. 109–136.

Sǎrler, B. (2005): A Radial Basis Function Collocation Approach in Computational Fluid Dynamics. *CMES: Computer Modeling in Engineering & Sciences*, vol. 7 (2), pp. 185–193.

Szady, M. J.; Salamon, T. R.; Liu, A. W.; Bornside, D. E.; Armstrong, R. C. (1995): A new mixed finite element method for viscoelastic flows governed by differential constitutive equations. *Journal of Non-Newtonian Fluid Mechanic*, vol. 59, pp. 215–243.

Tanner, R. I.; Xue, S.-C. (2002): Computing transient flows with high elasticity. *Korea-Australia Rheology Journal*, vol. 14, pp. 143–159.

Tran-Canh, D.; Tran-Cong, T. (2002): Computation of viscoelastic flow using neural networks and stochastic simulation. *Korea-Australia Rheology Journal*, vol. 14 (4), pp. 161–174.

Tran-Cong, T.; Mai-Duy, N.; Phan-Thien, N. (2002): BEM-RBF approach for viscoelastic flow analysis. *Engineering Analysis with Boundary Elements*, vol. 26 (9), pp. 757–762.

Xue, S. C.; Phan-Thien, N.; Tanner, R. I. (1995): Numerical study of secondary flows of viscoelastic fluid in strait pipes by an implicit finite volume method. *Journal of Non-Newtonian Fluid Mechanic*, vol. 59, pp. 191–213.

Zheng, R.; Phan-Thien, N.; Tanner, R. I.; Bush, M. B. (1990): Numerical analysis of viscoelastic flow through a sinusoidally corrugated tube using a boundary element method. *Journal of Rheology*, vol. 34 (1), pp. 79–102.

Table 1: Problem 2: Grid-convergence study at $We = 9$.

Grid	Relative L_2 errors		
	u_z	T_{zz}	T_{rz}
11×11	5.6228E-04	2.6259E-03	1.0973E-03
21×21	1.5928E-04	8.9349E-04	3.6454E-04
31×31	7.4343E-05	3.6953E-04	1.5495E-04
41×41	4.2581E-05	2.1614E-04	9.4571E-05
51×51	2.7541E-05	1.4178E-04	6.4001E-05

Table 2: Problem 3, Newtonian fluid: Comparison of the flow resistance fRe for $Re = 0$ computed for several values of ε and N

ε	0.1	0.1	0.2	0.286	0.3	0.5
N	0.5	0.1592	0.1042	0.2333	0.1592	0.5
			Present method			
21×21	17.71385	16.91518	19.75360	26.33921	26.40423	95.18132
41×41	17.73548	16.92656	19.76213	26.37003	26.42937	95.51616
61×61	17.74106	16.92760	19.76351	26.37759	26.43378	95.61778
SM [a]	17.7514	16.9290	19.7658	26.3724	26.437	95.6363
FCC [b]			19.765	26.383	26.437	
PSFD [c]			19.765	26.383	26.436	
PCFD [d]			19.761	26.377	26.432	

[a] Spectral method [Phillips and Owens (1997)]
[b] Fourier-Chebyshev Collocation [Pilitsis and Beris (1991)
[c] Pseudospectral/finite difference method [Pilitsis and Beris (1989)]
[d] Modified PSFD in a stretched cylindrical coordinate [Pilitsis and Beris (1989)]

Table 3: Problem 3, Newtonian fluid, $\varepsilon = 0.3$, $N = 0.16$: comparison of the flow resistance fRe for a wide range of *Re*

	Re									
	0	12	22.6	51	73	132	207.4	264	387.2	783
	Present method									
21×21	26.49503	27.22021	28.59313	31.80464	33.48944	36.61126	39.04828	40.34471	42.48868	46.02994
31×31	26.47991	27.20798	28.57514	31.78472	33.46705	36.56876	39.00632	40.29224	42.40401	45.66516
41×41	26.46953	27.19921	28.56523	31.77200	33.45333	36.53881	38.99009	40.27630	42.38337	45.62292
51×51	26.46298	27.19314	28.55838	31.76329	33.44396	36.51618	38.97686	40.26089	42.37057	45.60680
2D IRBFN [a]	26.4445	27.1773	28.5535	31.7511	33.4538	36.5424	38.996	40.3044	42.4595	45.7402
GFE [b]	26.4193	27.0911	28.4433	31.6984	33.4039	36.5392	38.933	40.1544	42.1112	45.0734
FCC [c]	26.4484	27.1791	28.5536	31.7484	33.4488	36.5264	38.9607	40.2446	42.3479	45.5828

[a] 2D-Integated Radial basis function network [Mai-Duy and Tanner (2006)]
[b] Galerkin finite element method [Pilitsis and Beris (1992)]
[c] Fourier-Chebyshev Collocation [Pilitsis and Beris (1992)]
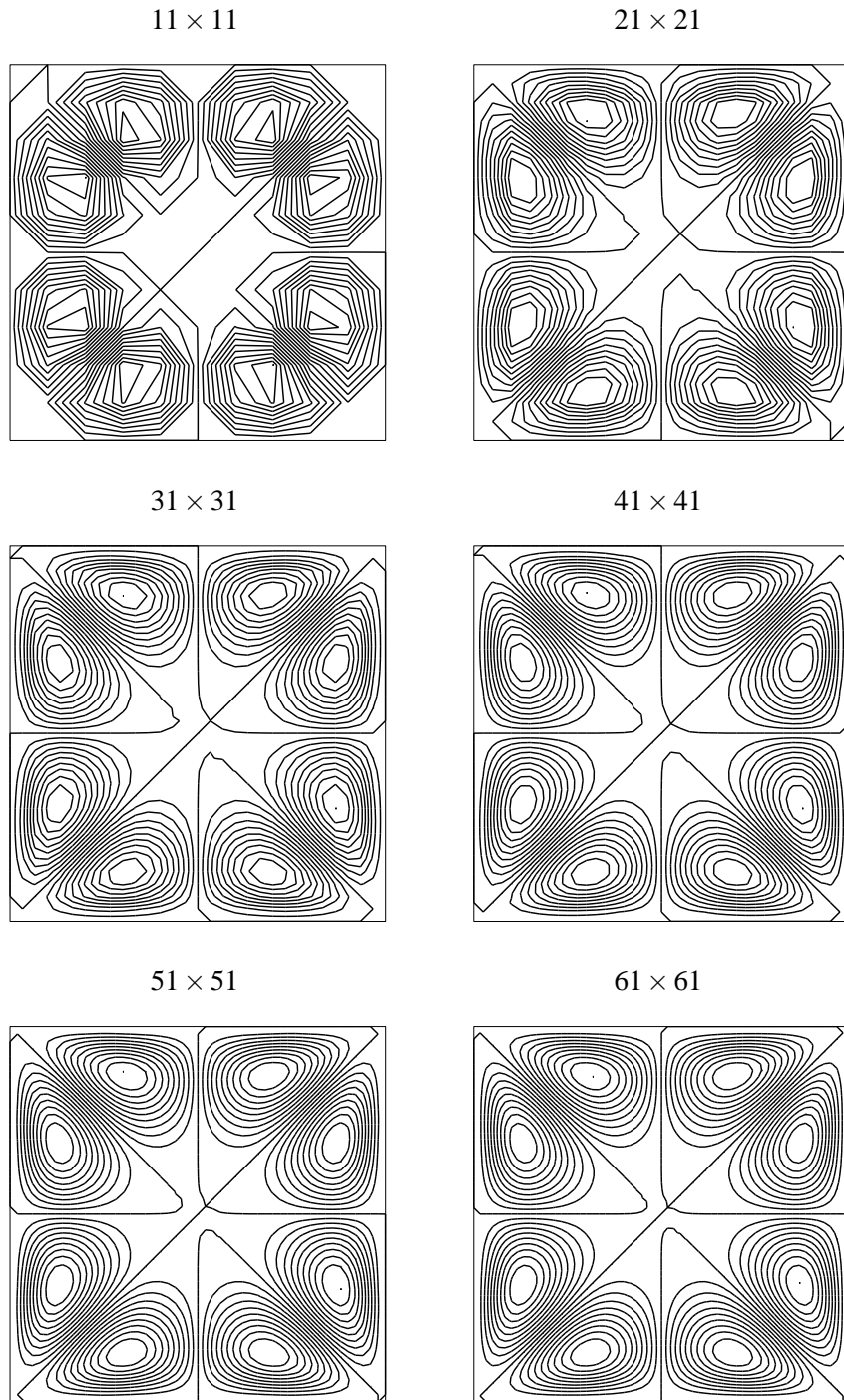
Figure 1: Problem 1: Convergence behaviour of the streamfunction field with respect to grid refinement.
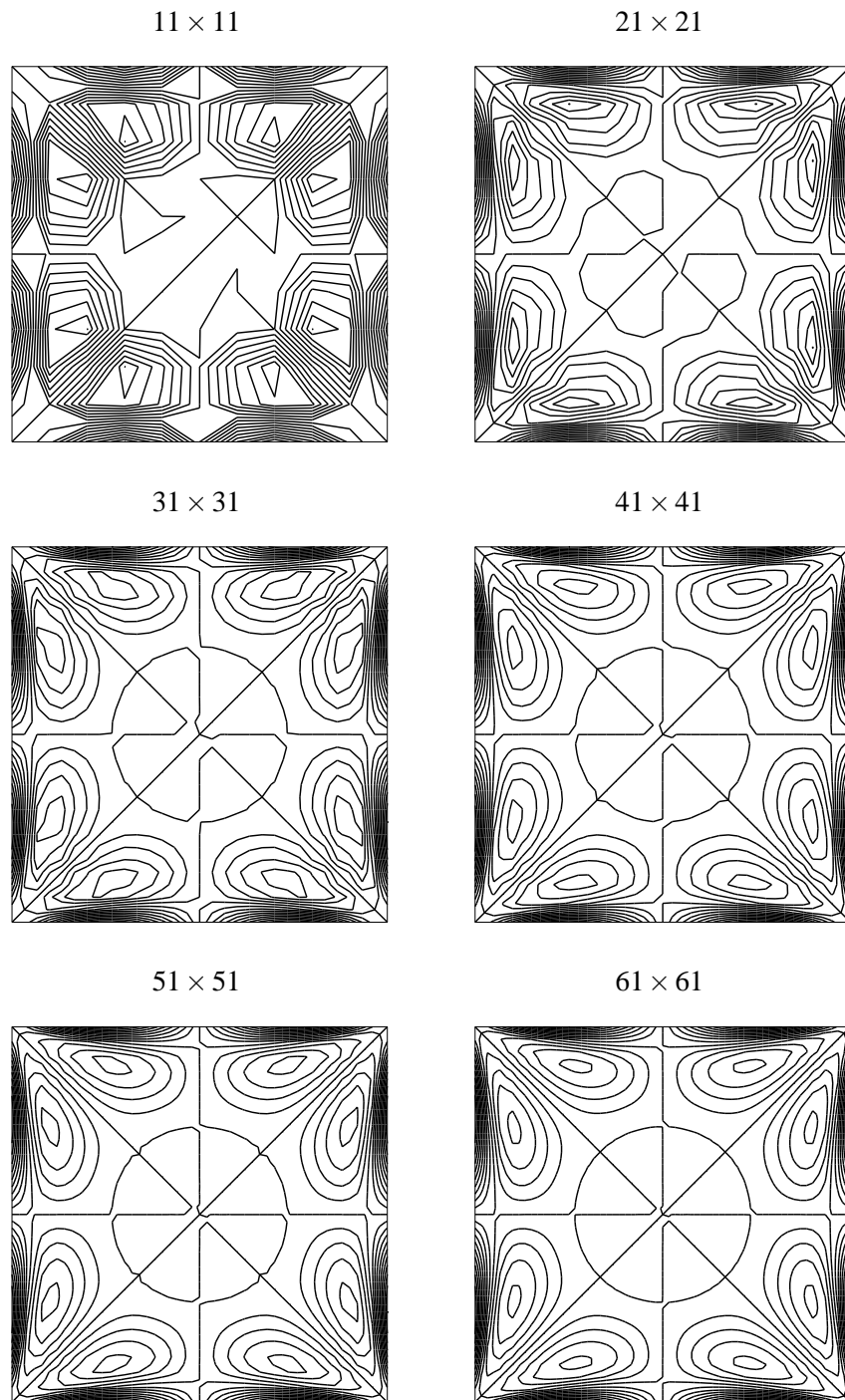
11×11

21×21

31×31

41×41

51×51

61×61

Figure 2: Problem 1: Convergence behaviour of the vorticity field with respect to grid refinement.

a) $\chi = 1.56$, 61×61

b) $\chi = 4$, 81×61

c) $\chi = 6.25$, 81×61
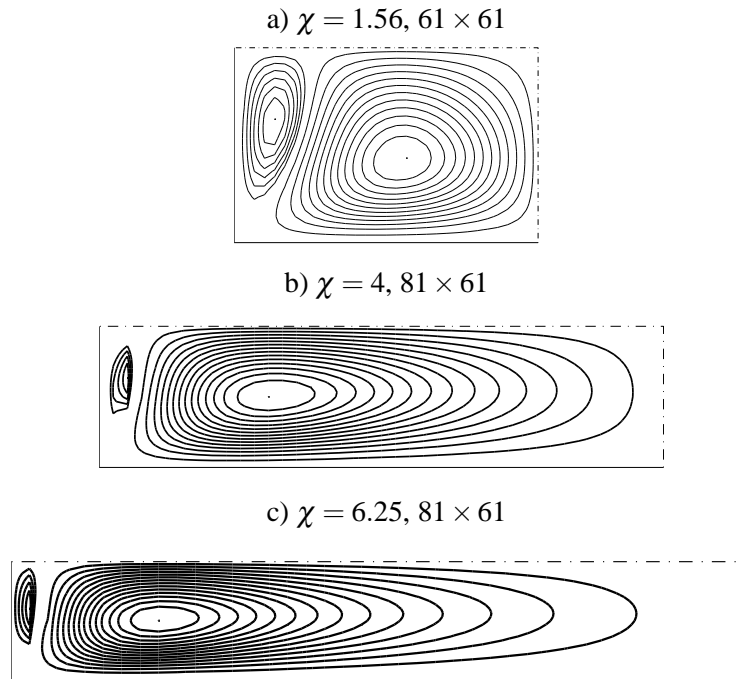
Figure 3: Problem 1: Streamlines of the secondary flow in one quarter of the cross-section computed for several values of the aspect ratio.

a) $\chi = 1.56$, 61×61

b) $\chi = 4$, 81×61

c) $\chi = 6.25$, 81×61
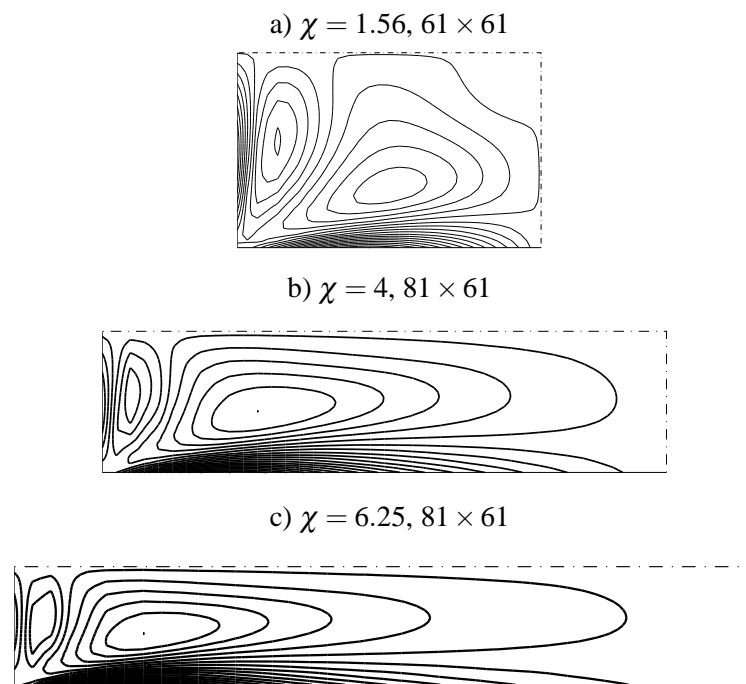
Figure 4: Problem 1: Contour plots for the vorticity in one quarter of the cross-section computed for several values of the aspect ratio.

a) $\chi = 1$, 61×61 b) $\chi = 1.56$, 61×61

c) $\chi = 4$, 81×61

d) $\chi = 6.25$, 81×61
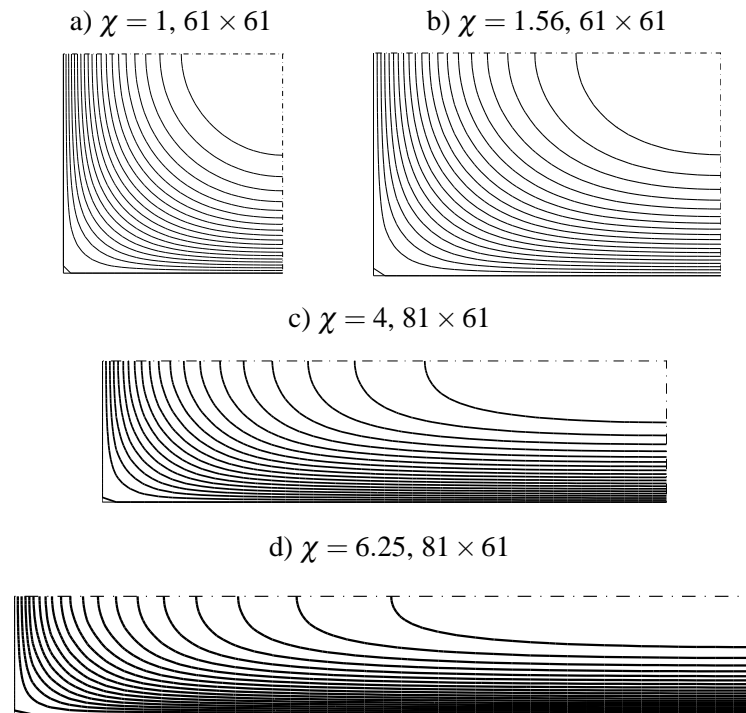
Figure 5: Problem 1: Contour plots for the primary velocity in one quarter of the cross-section computed for several values of the aspect ratio.

a) $\chi = 1$, 61×61 b) $\chi = 1.56$, 61×61

c) $\chi = 4$, 81×61

d) $\chi = 6.25$, 81×61
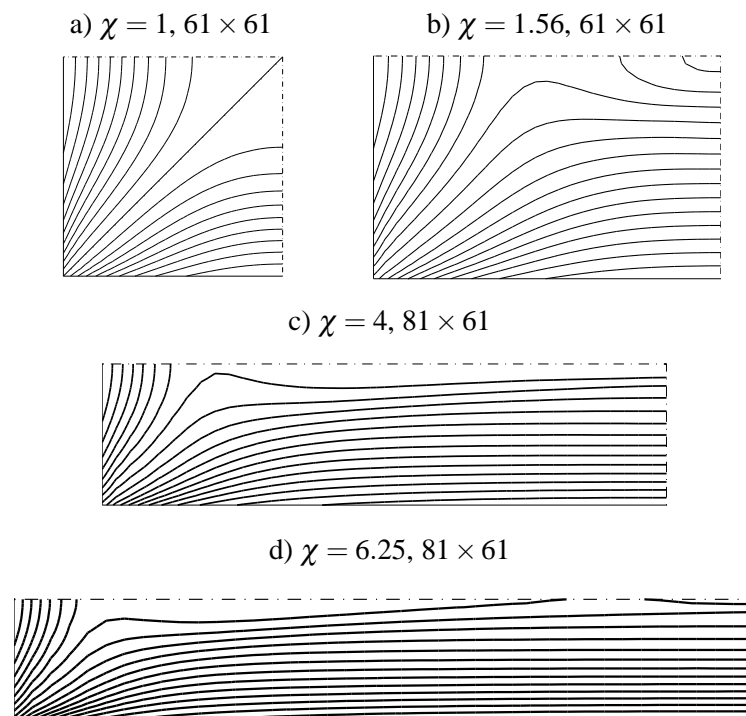
Figure 6: Problem 1: Contour plots for the second normal stress difference in one quarter of the cross-section computed for several values of the aspect ratio.
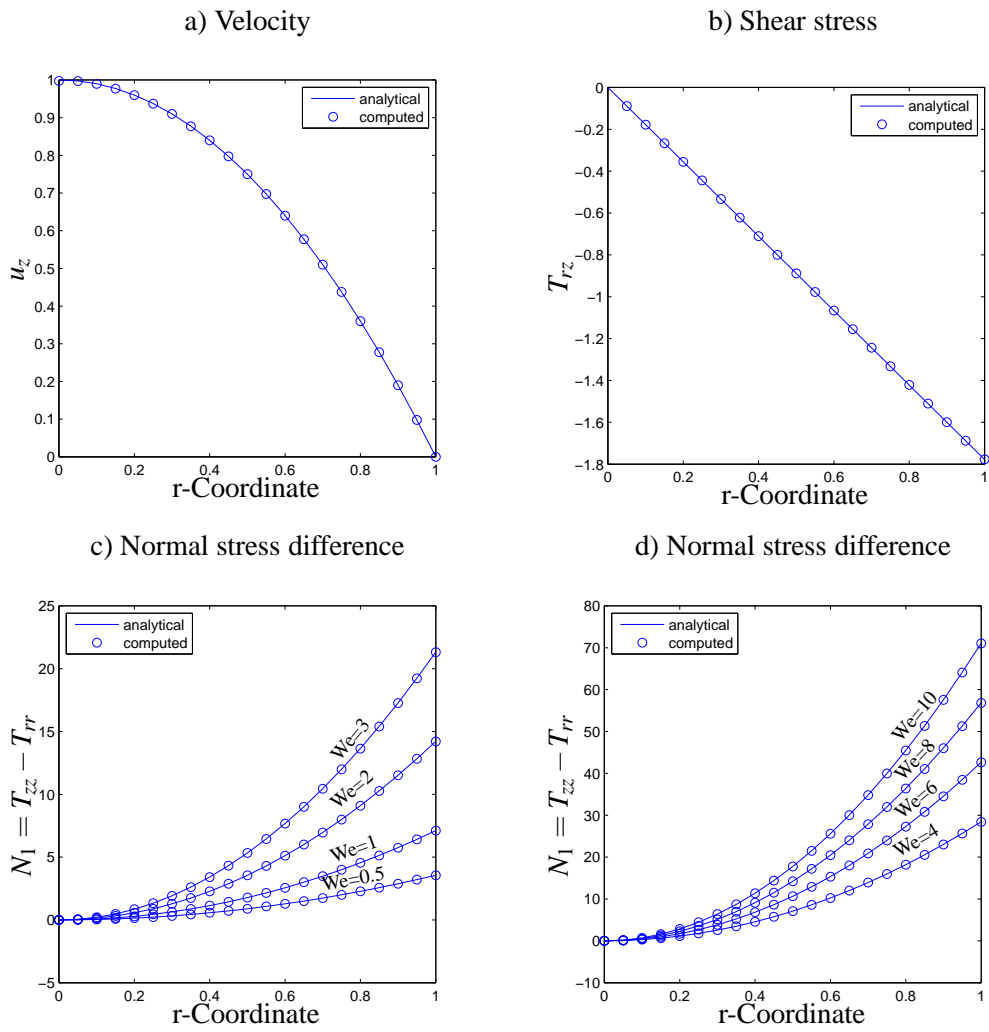
Figure 7: Problem 2: Profiles of velocity and stress on the middle plane $z = 0.5$ computed at several values of *We* using a grid of 21×21. It is noted that u_z and T_{rz} are independent of *We* and their corresponding computed results are indistinguishable.

a) Geometry
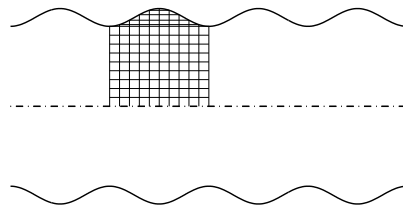
b) Reduced domain and discretisation
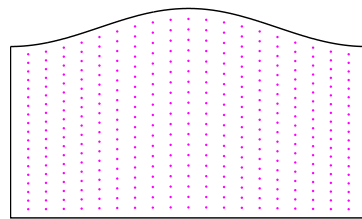
Figure 8: Problem 3: problem definition

ψ
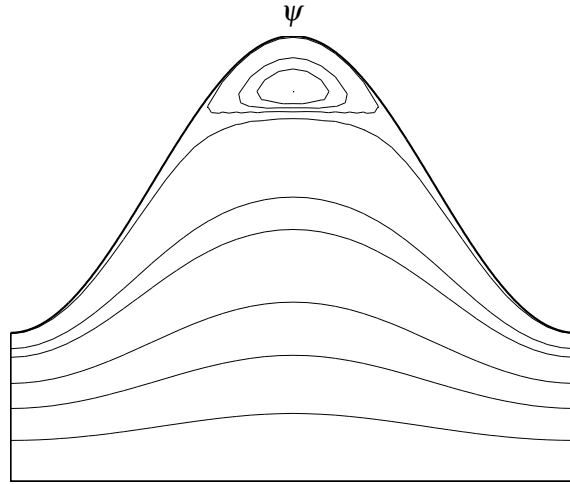
Figure 9: Problem 3, Newtonian fluid, $\varepsilon = 0.5$, $N = 0.5$, grid size $= 41 \times 41$: Streamlines for $Re = 0$. Iso-values used are 0, 0.02, 0.06, 0.1, 0.14, 0.15, 0.159. For $0.159157 \leq \psi \leq 0.15933$ an increment of 5.767×10^{-5} is used to resolve the recirculation region, which are the same as those in [Pilitsis and Beris (1991)].
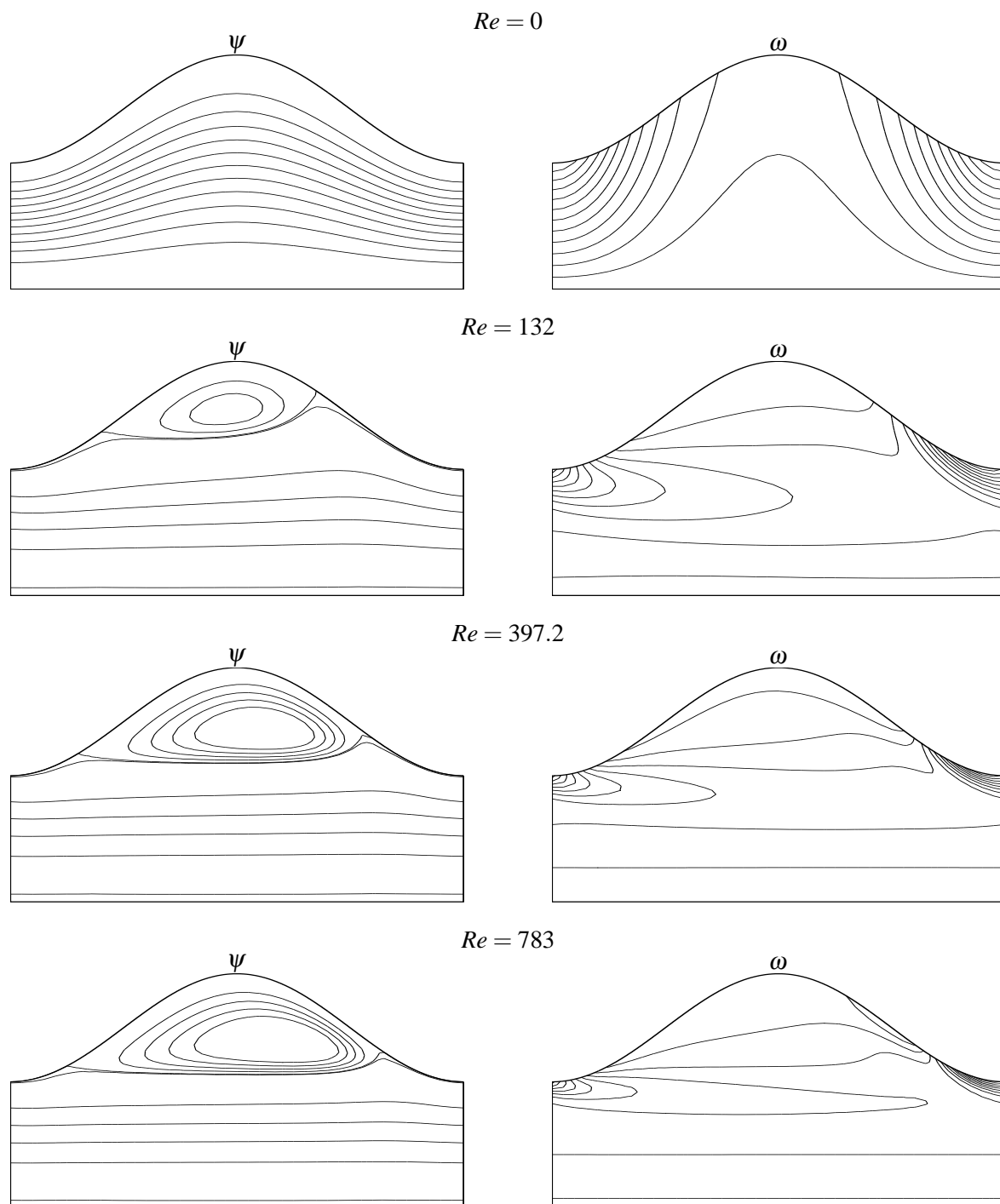
$Re = 0$

ψ

ω

$Re = 132$

ψ

ω

$Re = 397.2$

ψ

ω

$Re = 783$

ψ

ω

Figure 10: Problem 3, Newtonian fluid, $\varepsilon = 0.3$, $N = 0.16$, grid size $= 41 \times 41$: Contour plots of the stream-function and vorticity for a wide range of Re.
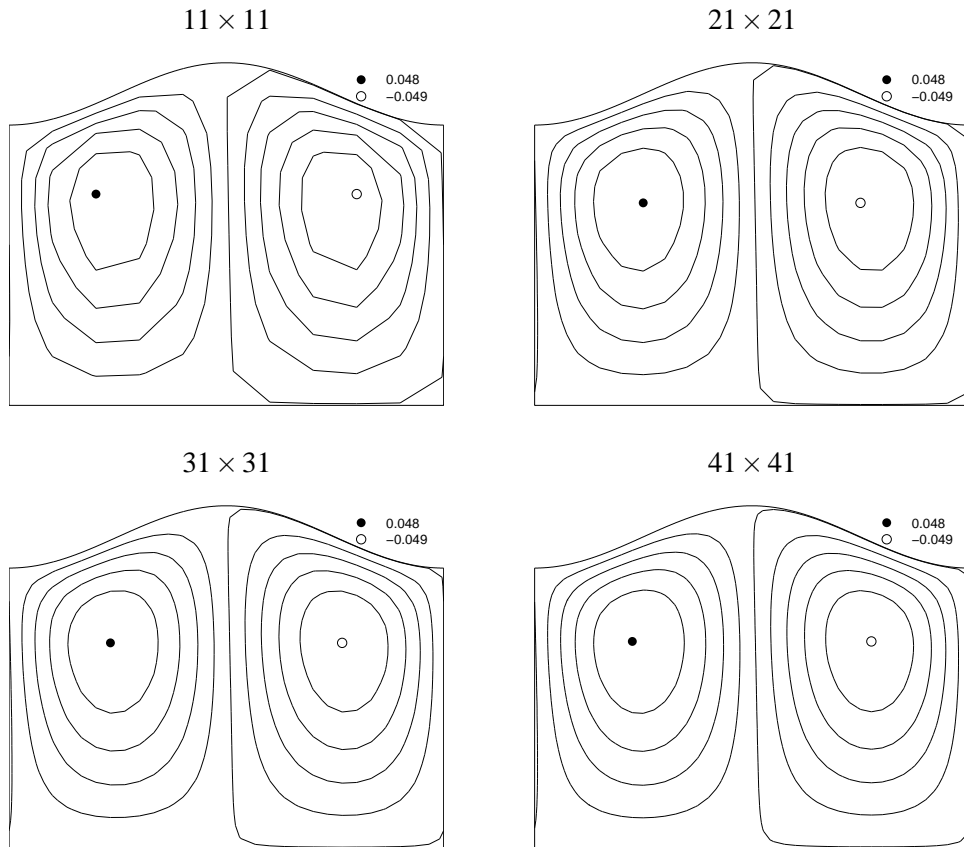
Figure 11: Problem 3, Oldroyd-B fluid, $\varepsilon = 0.1$, $N = 0.5$: Contour plots for u_r at $We = 2$ using several grids. The maximum and minimum values of u_r and their locations are also displayed.
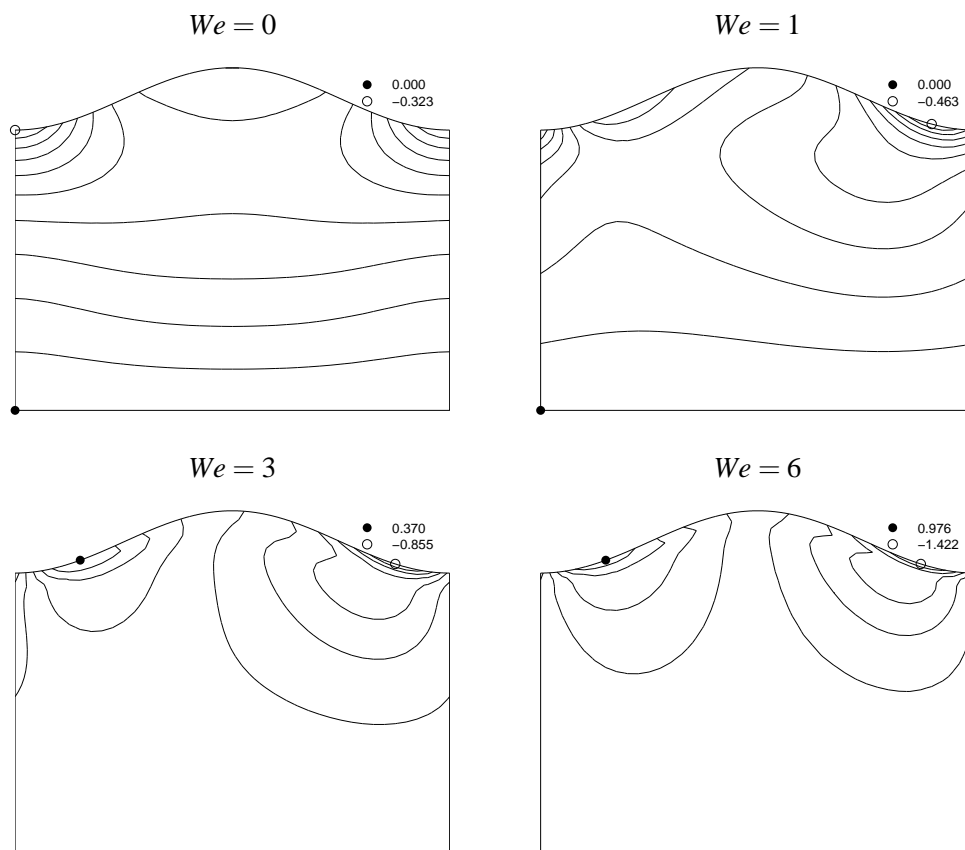
$We = 0$

$We = 1$

● 0.000
○ −0.323

● 0.000
○ −0.463

$We = 3$

$We = 6$

● 0.370
○ −0.855

● 0.976
○ −1.422

Figure 12: Problem 3, Oldroyd-B fluid, $\varepsilon = 0.1$, $N = 0.5$: Contour plots for T_{rz} at four values of We using a grid of 41×41. The maximum and minimum values of T_{rz} and their locations are also displayed.
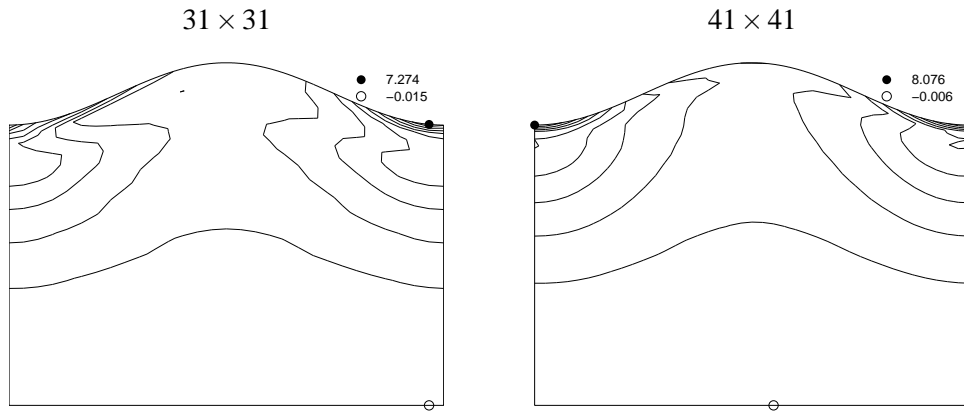
31×31 41×41

Figure 13: Problem 3, Oldroyd-B fluid, $\varepsilon = 0.1$, $N = 0.5$: Contour plots for T_{zz} at $We = 6$ using grids of 31×31 and 41×41. The maximum and minimum values of T_{zz} and their locations are also displayed.

a) $\varepsilon = 0.1$, $N = 0.5$
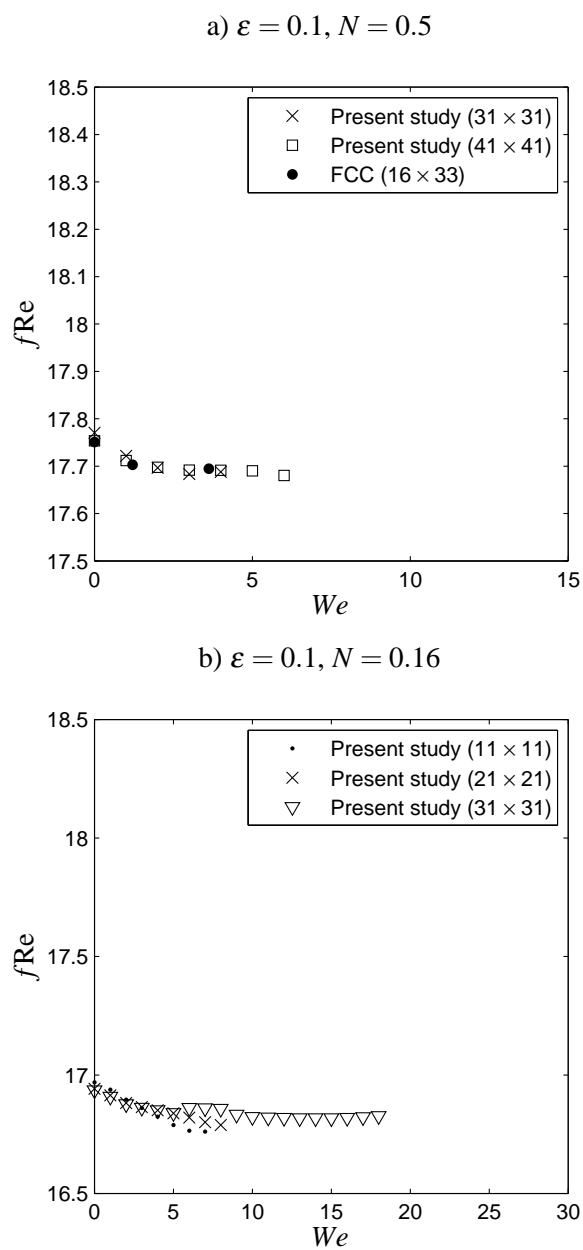

b) $\varepsilon = 0.1$, $N = 0.16$

Figure 14: Problem 3, Oldroyd-B fluid: The variation of the flow resistance with respect to the Weissenberg number for two geometrical configurations.